

# Magnetic injection photocurrents in valley polarized states of twisted bilayer graphene

Fernando Peñaranda,<sup>1</sup> Héctor Ochoa,<sup>2</sup> and Fernando de Juan<sup>1,3</sup>

<sup>1</sup>Donostia International Physics Center, P. Manuel de Lardizabal 4, 20018 Donostia-San Sebastian, Spain

<sup>2</sup>Department of Physics, Columbia University, New York, NY 10027, USA

<sup>3</sup>IKERBASQUE, Basque Foundation for Science, Plaza Euskadi 5, 48009 Bilbao, Spain

(Dated: January 17, 2025)

Magic-angle twisted bilayer graphene displays a complex phase diagram as a function of flat band filling, featuring compressibility cascade transitions and a variety of competing ground states with broken spin, valley and point group symmetries. Recent THz photocurrent spectroscopy experiments have shown a dependence on the filling which is not consistent with the simplest cascade picture of sequential filling of equivalent flat bands. In this work, we show that when time-reversal symmetry is broken due to valley polarization, a magnetic injection photocurrent develops which can be used to distinguish different spin-valley polarization scenarios. Using the topological heavy fermion model we compute both shift and injection currents as a function of filling and argue that current experiments can be used to determine the spontaneous valley polarization.

*Introduction* - Magic-angle twisted bilayer graphene (TBG) [1] is a unique correlated electron system displaying a wide variety of broken-symmetry ground states [2–10] and unconventional superconductivity [11–13]. These states originate from the partial filling of spin and valley degenerate flat bands, where the enhanced Coulomb interaction favors competing states with different flavor polarization. Some of these states are believed to be time-reversal symmetry breaking spin and orbital magnets displaying the anomalous Hall effect, which has been reported at odd fillings  $\nu = 1, 3$  in the electron [6–8] and hole sides [14], and under some circumstances near  $\nu = 2$  [10]. These states appear to emerge from a parent high-temperature state where the different flavours are filled sequentially as a function of carrier density, causing a periodic reset of the chemical potential known as cascade behavior, observed both in local tunneling [15–18] and compressibility [19, 20]. Since the cascade behaviour remains up to much higher temperatures (20–30 K) [18–20] than those where insulating states develop at integer fillings, the cascade itself does not necessarily signal symmetry breaking [21, 22], while the AHE does.

Photocurrent THz spectroscopy [23–25] is a unique optical probe [26, 27] to examine the symmetry and quantum geometry of TBG flat bands [28–34], and can offer a unique insight regarding the breaking of time reversal symmetry. Recent experiments have shown photocurrents are sensitive to the cascade behaviour [35], albeit with low temperature sign-changing features which are inconsistent with a naive periodic resetting of the chemical potential. This suggests that photocurrents are sensitive to the flavor polarization realized at each filling.

In this work, we propose that a particular photocurrent mechanism known as magnetic injection current [36–44] which switches sign with magnetization, is the dominant one in the valley polarized states and may be responsible for the observations. Using the topological heavy fermion model (see sketch in Fig. 1 a), we compute both shift and injection currents for continuously varying flat

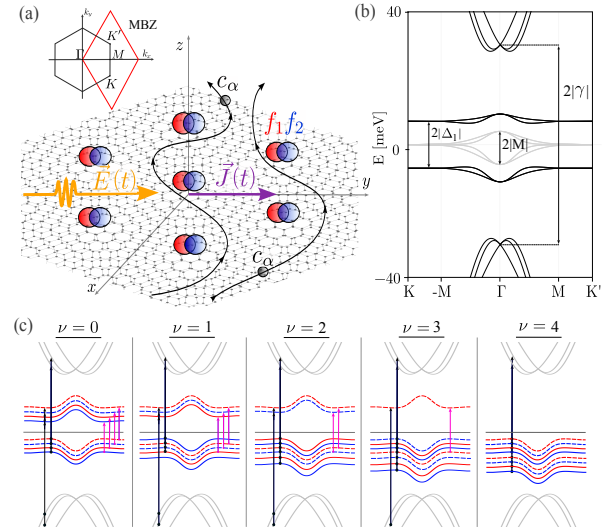


FIG. 1. (a) Sketch of a TBG flake in the presence of an incident in-plane electric field  $E(t)$  and the resulting induced non-linear current  $J(t)$ . The two local  $f$  orbitals (per valley and spin) in the heavy fermion description of TBG are depicted in red and blue at the AA positions of the moiré pattern, whereas the  $c$  electrons of the delocalized conduction bands are shown in black. The high symmetry points of the moiré Brillouin zone (MBZ) are shown in the figure inset. (b) Bands of the non-interacting THFM close to magic angle in the absence (gray) and presence (black) of a layer-even sublattice mass. (c) Schematic of the allowed optical transitions between occupied and unoccupied bands at integer  $\nu$ . Flat to flat (FF) transitions are depicted in pink and flat to dispersive (FD) in black. Solid and dashed, and red and blue encode different valley and spin flavors, respectively.

band filling in the Hartree-Fock approximation, and discuss how these two contributions may be separated from symmetry considerations.

*Bulk photovoltaic effects* - In non-centrosymmetric systems in the presence of constant light irradiation, a DC

photocurrent is generated with the general form

$$J_i = \sigma_{ijk}(E_j E_k^* + E_j^* E_k) + i\eta_{ijk}(E_j E_k^* - E_j^* E_k), \quad (1)$$

where  $\sigma_{ijk} = \sigma_{ikj}$  denotes the linear PGE while  $\eta_{ijk} = -\eta_{ikj}$  denotes the circular PGE. Both effects are generated via two main mechanisms known as shift and injection currents [45]. Focusing only on LPGE, relevant to current experiments, we have  $\sigma_{ijk} = \sigma_{ijk}^{\text{sh}} + \sigma_{ijk}^{\text{inj}}$  where

$$\sigma_{ijk}^{\text{sh}} = \frac{\pi e^3}{2\hbar^2} \int_{\mathbf{k}} \sum_{nm} f_{nm} \text{Im}[r_{nm}^k; i r_{mn}^j - r_{nm}^k r_{mn}^j; i] \delta(\omega - \omega_{nm}), \quad (2)$$

$$\sigma_{ijk}^{\text{inj}} = \tau \frac{\pi e^3}{\hbar^2} \int_{\mathbf{k}} \sum_{nm} f_{nm} \partial_{k_i} \omega_{nm} \text{Re}[r_{nm}^j r_{mn}^k] \delta(\omega - \omega_{nm}), \quad (3)$$

and  $\tau$  is the scattering time.  $\sigma_{ijk}^{\text{sh}}$  is a  $\mathcal{T}$ -even response while  $\sigma_{ijk}^{\text{inj}}$  is a  $\mathcal{T}$ -odd response which occurs only in magnetic systems and switches sign when polarization is reversed. When electronic excitations can be described in terms of independent valleys related by time-reversal symmetry, as in TBG, the magnetic injection current can be seen as a valley photocurrent [29, 46], which becomes a true charge photocurrent once time reversal symmetry is broken. In clean magnetic systems with large  $\tau$ , the injection current dominates over the shift current.

The different photocurrent components are strongly constrained by the lattice point group  $D_6$  of TBG, which in fact forbids all photocurrents at normal incidence [33] ( $i, j, k = x, y$ ). The experimental observation of such photocurrents, once photo-thermoelectric and other effects are excluded, implies that the  $C_{2z}$  symmetry is broken. Since photocurrents are observed up to 60 K, which is much higher than the temperature scale of correlation effects,  $C_{2z}$  symmetry breaking must be external and come from the substrate. This reduces the symmetry to just  $C_{3z}$  and enables two independent components of the shift current  $\sigma_{yyy} = -\sigma_{yxx} = -\sigma_{xxy}$ , and  $\sigma_{xxx} = -\sigma_{xyy} = -\sigma_{yyx}$  [28–31]. Symmetry requires that to leading order,  $\sigma_{yyy}$  is proportional to the layer even part of the sublattice potential, while  $\sigma_{xxx}$  is proportional to the layer odd part [33].

*Correlated ground states* - The low-temperature phase diagram of TBG as a function of flat-band filling remains a debated subject, with several ground state candidates predicted for different fillings. Low temperature symmetry breaking states be divided into two classes depending on what density matrix expectation values are non-zero in the sublattice or Chern basis: polarized states (with diagonal density matrices) vs coherent states (with off-diagonal density matrices). This distinction is important because while coherent states like the Kramers Intervalley Coherent (KIVC) [47] and the Incommensurate Kekule Spiral (IKS) [48] are competitive

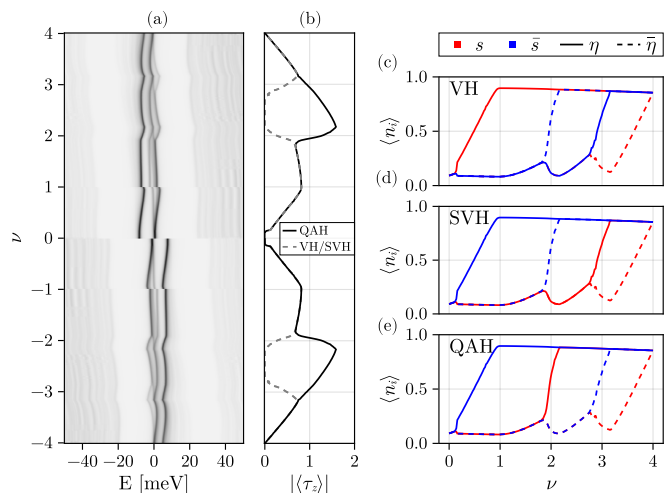


FIG. 2. Sequence of mean-field ground states as a function of filling in the THFM: (a) Normalized density of states referred to the Fermi surface as a function of filling. (b) Valley polarization as a function of the filling. (c-e) Occupation of the flat bands vs filling for three distinct ground states corresponding to VH (c), SVH (d), and QAH (e) phases. Red and blue colors and solid and dashed lines encode different spin and valley flavors, respectively. Parameters:  $U = 5$  meV,  $\Delta_1 = 2.5$  meV and  $J = 1$  meV.

ground states in the absence of an hBN substrate, the substrate induced potential strongly favors only polarized states [48–50]. These states can be characterized by what flavors (spin and valley) are filled, with each flavor having a Chern number given by the product of the sublattice and valley eigenvalue [36, 50–52]. Filling an odd number of bands always leads to a spin and valley polarized Chern insulator with  $|C| = 1$ , while for filling  $\nu = 2$ , a valley polarized Quantum Anomalous Hall (QAH) state with  $C = 2$ ,  $|\uparrow +, \downarrow +\rangle$ , is nearly degenerate with a ferromagnetic valley Hall (VH)  $|\uparrow +, \uparrow -\rangle$  and spin-valley Hall (SVH)  $|\uparrow +, \downarrow -\rangle$  states with zero Chern number [50, 53, 54]. Other symmetry breaking states like nematic semimetals [55, 56] and stripe phases [55, 57] are also predicted, as well as symmetry preserving Mott and symmetric Kondo [58–61] states, which may be realized at higher temperatures. Here we focus only on the polarized states favored by the substrate.

As explained above, all states that break time-reversal symmetry should have an extra photocurrent coming from magnetic injection in Eq. 3. This is true for all odd-filling states, while for half-filling it depends on the state: The QAH state does break time-reversal symmetry, while the SVH preserves it, and the VH preserves a spinless time-reversal symmetry. Magnetic injection is thus forbidden in VH and SVH. Finally, it is also worth noting that TBG has an approximate particle-hole symmetry (PHS) [47, 62–67] which leads to important constraints for the photocurrent [33], which as we will demonstrate are realized even in the correlated states.

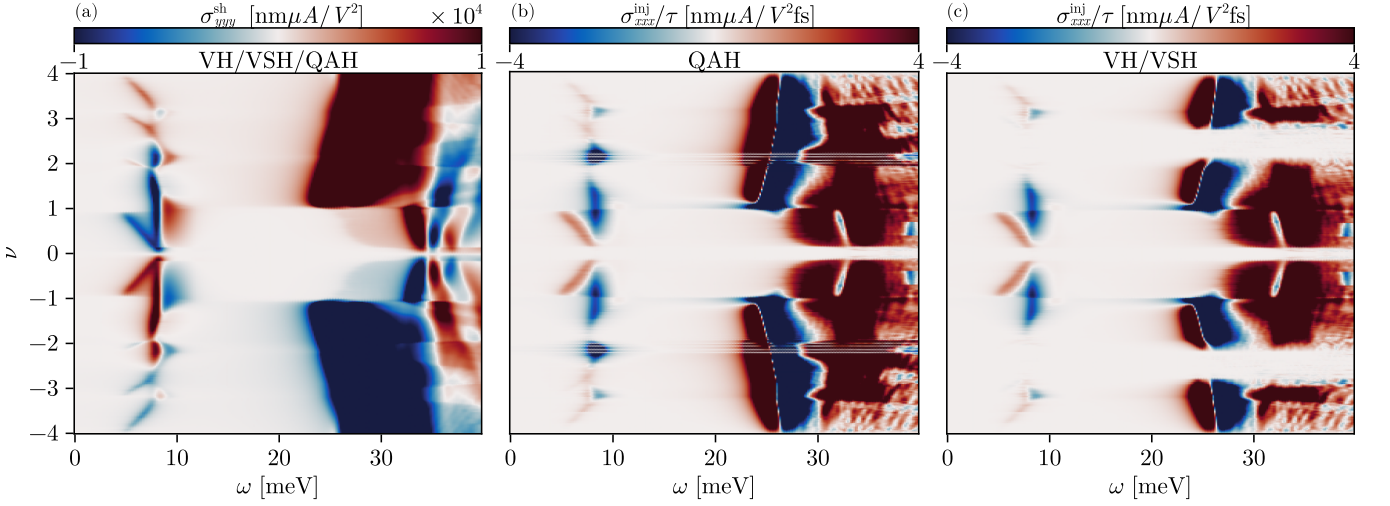


FIG. 3. (a) Shift and (b,c) magnetic injection components as a function of frequency and filling in the presence of a layer-even sublattice mass  $\Delta_1 = 2.5$  meV for the different interacting ground states described in Fig. 2. Whereas the QAH, VH, and SVH phases give rise to the same  $\sigma_{yy}^{shift}$ , those with different Chern number: 0 (VH/SVH) and 2 (QAH), lead to a different  $\sigma_{xx}^{inj}$  response near  $\nu = 2$  in (b) and (c), respectively. Same parameters as in Fig. 2.

*Heavy fermion model* - To compute the photocurrent spectrum in the correlated states we consider the topological heavy fermion model (THFM) of TBG [68], which is a faithful representation of the continuum model [1, 69] that separates the degrees of freedom into localized, strongly interacting states  $f$  and extended, topological states  $c$  (see Fig. 1(a)). The single-particle THFM is given by:

$$\begin{aligned} \hat{H}_0 = & \sum_{|\mathbf{k}| < \Lambda_c} \sum_{a, a', \eta, s} \left( H_{aa'}^{(c, \eta)}(\mathbf{k}) - \mu \delta_{aa'} \right) \hat{c}_{\mathbf{k}a\eta s}^\dagger \hat{c}_{\mathbf{k}a'\eta s} \\ & - \mu \sum_{\eta s} \sum_{\mathbf{R}} \hat{f}_{\mathbf{R}\alpha\eta s}^\dagger \hat{f}_{\mathbf{R}\alpha\eta s} + \frac{1}{\sqrt{N}} \times \\ & \times \sum_{|\mathbf{k}| < \Lambda_c, \mathbf{R}} \left[ e^{i\mathbf{k} \cdot \mathbf{R} - \frac{|\mathbf{k}|^2 \lambda^2}{2}} H_{\alpha\alpha}^{(f, c, \eta)}(\mathbf{k}) \hat{f}_{\mathbf{R}\alpha\eta s}^\dagger \hat{c}_{\mathbf{k}\alpha\eta s} + H.c. \right], \end{aligned} \quad (4)$$

where  $\hat{c}_{\mathbf{k}a\eta s}^\dagger$  ( $\hat{c}_{\mathbf{k}a\eta s}$ ) creates (destroys) a  $c$  electron in conduction band  $a \in \{1, 2, 3, 4\}$  with spin  $s$ , valley  $\eta$ , and momentum  $\mathbf{k}$  smaller than the  $c$ -electron momentum cutoff  $\Lambda_C$  [70], while  $\hat{f}_{\mathbf{R}\alpha\eta s}^\dagger$  ( $\hat{f}_{\mathbf{R}\alpha\eta s}$ ) creates (destroys) an  $f$  electron with orbital  $\alpha \in \{1, 2\}$  at the moiré unit cell located at position  $\mathbf{R}$ , with spin  $s$  and valley  $\eta$ .  $N$  denotes the number of moiré unit cells,  $\mu$  the chemical potential, and  $\lambda = 0.3375a_M$  a damping factor proportional to the spread of the local orbitals with  $a_M$  the moiré lattice constant.  $H^{(cc, \eta)}$  is the non-interacting Hamiltonian for the  $c$  electrons:

$$H^{(cc, \eta)} = \begin{pmatrix} 0_{2 \times 2} & v_\star(\eta k_x \sigma_0 + i k_y \sigma_z) \\ v_\star(\eta k_x \sigma_0 - i k_y \sigma_z) & M \sigma_x \end{pmatrix}, \quad (5)$$

and

$$H^{(f, c, \eta)}(\mathbf{k}) = [\gamma \sigma_0 + v'_\star(\eta k_x \sigma_x + k_y \sigma_y), 0_{2 \times 2}], \quad (6)$$

captures the  $f$ - $c$  hybridization responsible for two isolated flat-bands with bandwidth  $2|M|$  separated from the dispersive bands by  $|\gamma| - |M|$ . The resulting bandstructure is shown in Fig. 1(b).  $v_\star$ ,  $v'_\star$ ,  $M$ , and  $\gamma$  values are obtained from the continuum model parameters at a twist angle  $\theta = 1.05$  [68].

The leading order effect of the substrate is to exert independent sublattice potentials for top and bottom layer, with moiré effects playing a secondary role [71, 72], and this model is often used in continuum model calculations [29, 31, 35]. In the THFM a layer-even sublattice potential corresponds by symmetry to  $f$ -fermion orbital polarization  $\sigma_z$ , which opens a gap and generates the expected Chern bands. The layer-odd sublattice potential, on the other hand, does not correspond to any constant matrix in the  $f$  or  $c$  fermion space. Symmetry analysis, as well as an explicit projection, reveals the layer-odd sublattice mass to be a nearest neighbor  $\sigma_z$  hopping operator, leading to the overall substrate potential:

$$\hat{H}_{\text{subs}} = \sum_{\mathbf{R}} \sum_{\alpha s \eta} \left( \Delta_1 \sigma_z + \Delta_2 \xi \sum_{i=1}^3 \sin(\mathbf{k} \cdot \mathbf{a}_i) \sigma_z \right) \hat{f}_{\mathbf{R}\alpha s \eta}^\dagger \hat{f}_{\mathbf{R}\alpha s \eta}, \quad (7)$$

where  $\Delta_1$  is the layer even mass, and  $\Delta_2$  is the layer-odd one, and  $\xi^{-1} = 2 \sin\left(\frac{-\pi}{\sqrt{3}}\right) + \sin\left(\frac{2\pi}{\sqrt{3}}\right)$ . The band structure in the presence of finite  $\Delta_1$  is shown in Fig. 1(b), where the usual opening of a gap is appreciated.

Adding correlations to the THFM is achieved by projecting the screened Coulomb interaction into the  $f$  and

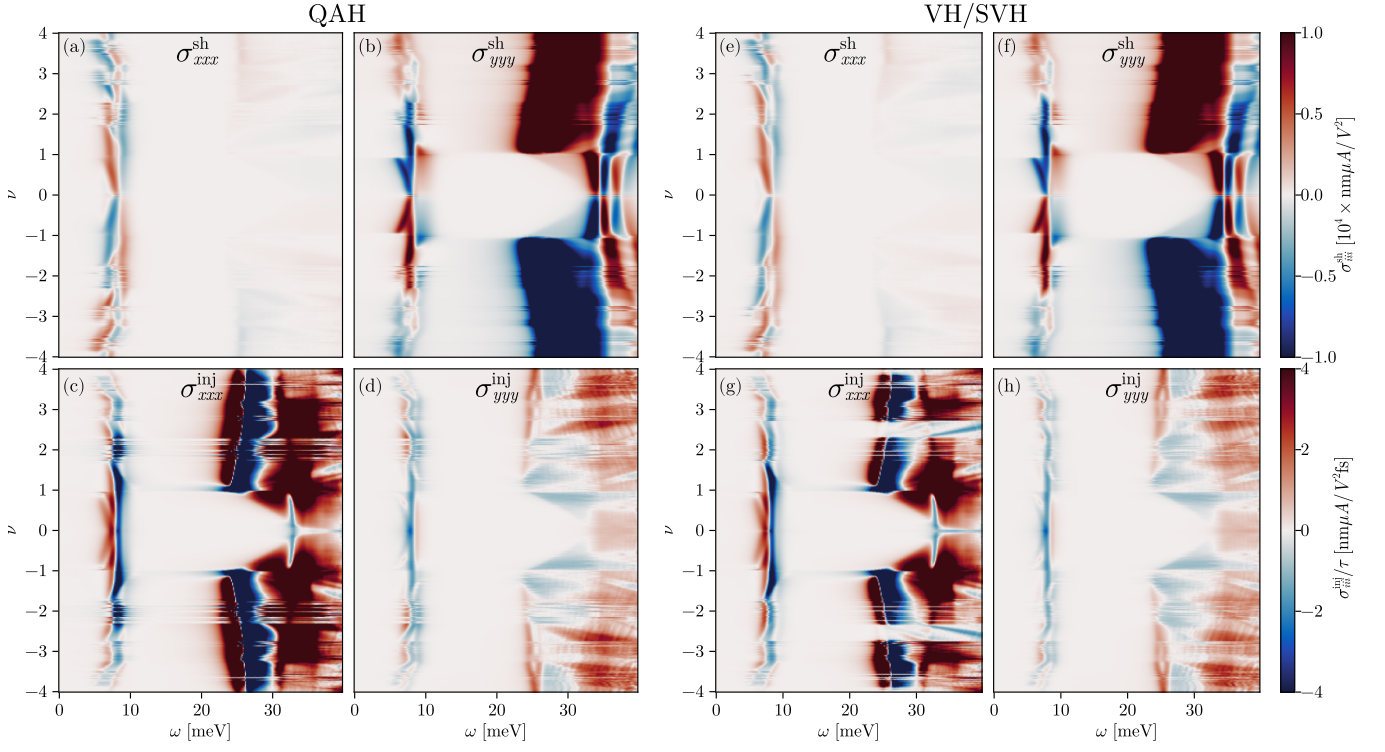


FIG. 4. In-plane photocurrents in the presence of a layer-odd sublattice mass for the QAH (a-d) and VH/SVH (e-h) phases as a function of frequency and filling. (a,e)  $\sigma_{xxx}^{\text{sh}}$  (b,f)  $\sigma_{yyy}^{\text{sh}}$  (c,g)  $\sigma_{xxx}^{\text{inj}}$  and (d,h)  $\sigma_{yyy}^{\text{inj}}$ . Parameters:  $\Delta_1 = 2.5$  meV,  $\Delta_2 = 1$  meV, the rest as in Fig. 3.

$c$  degrees of freedom. This leads to a density-density interaction between  $f$  electrons  $\hat{H}_U$  parametrized by  $U$  and an exchange-like interaction  $\hat{H}_J$  between  $f$  and  $c$  electrons parametrized by  $J$ , in close resemblance to a generalized Anderson model. To leading order in the interaction strengths a Hartree-Fock decoupling of such two terms leads to:

$$\hat{H}_U = -\frac{NU}{2} (\nu_f^2 + 8\nu_f - \text{Tr}[O^f O^f]) + U \sum_{\mathbf{R}} \sum_{\alpha\eta} \sum_{\alpha's'\eta'} \left[ (\nu_f + \frac{1}{2}) \delta_{\alpha\alpha'} \delta_{ss'} \delta_{\eta\eta'} - O_{\alpha\eta, \alpha's'\eta'}^f \right] \hat{f}_{\mathbf{R}\alpha's'\eta'}^\dagger \hat{f}_{\mathbf{R}\alpha\eta} \quad (8)$$

and

$$\hat{H}_J = -\frac{J}{2} \sum_{|\mathbf{k}| < \Lambda_C} \sum_{\alpha\eta} \sum_{\alpha's'\eta'} \left[ (\eta\eta' + (-1)^{\alpha+\alpha'}) \times \left( O_{\alpha\eta s, \alpha's'\eta's'}^f - \frac{1}{2} \delta_{\alpha\alpha'} \delta_{ss'} \delta_{\eta\eta'} \right) \right] \hat{c}_{\mathbf{k}, \alpha'+2, \eta's'}^\dagger \hat{c}_{\mathbf{k}, \alpha+2, \eta s} \quad (9)$$

where  $O_{\alpha\eta, \alpha's'\eta'}^f = \langle \psi | f_{\mathbf{R}\alpha\eta}^\dagger f_{\mathbf{R}\alpha's'\eta'} | \psi \rangle$  is the density matrix of the  $f$  electrons, in terms of the interacting mean-field ground state  $\psi$ , and  $\nu_f = \text{Tr}[O^f] - 4$ .

Fig. 2 shows the ground states as function of filling, computed self-consistently within the THFM. The existence of the periodic resets in chemical potential can be seen in the DOS in Fig. 2(a), and the evolution of the valley polarization is shown in 2(b). Fig 2(c) shows the partial filling of the spin and valley polarized bands for each of the three choices, QAH, VH, and VSH.

*Photocurrent results* - We first consider the simplified case where the substrate induces a layer-even sublattice potential and the  $C_{2y}$  axis is preserved. In the presence of valley polarization (which breaks  $C_{2y}$  and  $\mathcal{T}$  but preserves their product  $C_{2y}\mathcal{T}$ ), magnetic injection is allowed only in  $\sigma_{xxx}^{\text{inj}}$  and shift in  $\sigma_{yyy}^{\text{sh}}$  while  $\sigma_{xxx}^{\text{sh}} = \sigma_{yyy}^{\text{inj}} = 0$  due to  $C_{2y}\mathcal{T}$ . This limiting case thus has the interesting feature that injection and shift currents can be distinguished by their direction. Fig. 3 shows  $\sigma_{xxx}^{\text{inj}}$  and  $\sigma_{yyy}^{\text{sh}}$  as a function of their filling and frequency, in a range than includes optical transitions between flat bands (FF) (5-15 meV) and between flat and dispersive bands (FD) (20-40 meV), schematically shown in Fig. 1(c). Both photocurrents show much stronger FD transitions compared to FF transitions, as found previously without valley polarization [29, 31, 33], but their detailed dependence is however different, showing several sign changes in both frequency and filling.  $\sigma_{yyy}^{\text{sh}}$  is insensitive to the particular polarization (QAH/VH/SVH), while  $\sigma_{xxx}^{\text{inj}}$  does show a dependence, vanishing at half-filling in the case of the

VH/VSH states as expected. Fig. 3 also shows that the shift current is odd under filling reversal, a direct consequence of PHS. Similarly the injection current, assuming the same sign of valley polarization through the filling cascade, is even under filling reversal.

For a more realistic account of the effect of the substrate we now add a finite layer-odd potential  $\Delta_2$ . In this case, only  $C_{3z}$  remains and both  $\sigma_{xxx}^{\text{sh}}$  and  $\sigma_{yyy}^{\text{inj}}$  become allowed. Fig. 4 shows both cases for the different polarization sequence. In general, we observe that  $\sigma_{xxx}^{\text{inj}}$  and  $\sigma_{yyy}^{\text{sh}}$  remain the dominant components with similar features as in Fig. 3, while  $\sigma_{yyy}^{\text{inj}}$  and  $\sigma_{xxx}^{\text{sh}}$  are smaller.

*Discussion* - In our work, we have predicted a magnetic injection photocurrent in TBG which becomes enabled due to spontaneous valley polarization. The most distinctive feature of such photocurrent is that it is magnetically switchable [36]: the time-reversed ground state (i.e. with opposite valley polarization) should have an opposite photocurrent. Since valley polarization is a time-odd  $B_1$  irrep of  $D_6$ , it should be switchable with an in-plane magnetic field [73–75], which to cubic order contains the time-odd  $B_1$  irrep  $B_x^3 - 3B_x B_y^2$ . An alternative way could be to use current pulses [76–78], which were shown to flip the AHE experimentally [7, 8]. Either method may serve to isolate the injection current by subtracting the signal with opposite polarizations, and also to check prediction that the injection current is odd under filling reversal keeping constant polarization. Another key feature of the injection current is that it grows with the scattering time  $\tau$  while the shift current does not, so cleaner samples should show stronger injection currents.

The injection photocurrent neatly discriminates between topological QAH and trivial VH and VSH states, which are degenerate in energy within the THFM. Their degeneracy is only lifted by a valley-spin Hund coupling removing the independent spin rotational symmetry of each valley, with a magnitude and sign which is under debate as both Coulomb scattering between valleys and electron-phonon coupling with K-valley phonons can contribute [79]. Thus, the injection current can be a useful probe to discern the dominance of these mechanisms.

To compare our theory with the experimental observation of bulk photocurrents [35], a number of caveats should be taken into account. Photocurrents have been measured both in insulating and metallic samples at neutrality [35], suggesting  $C_{2z}$  breaking perturbations are inhomogeneous [80, 81] and not always lead to a global gap. This implies that photocurrent patterns will vary across the sample, making an estimation of the sublattice potential challenging. In addition, the crystallographic direction in these experiments is not currently known, and strain effects may also play a role in the breaking of symmetries. While a more systematic study is required to isolate the injection current in the experiment, we believe the sign changes which have been observed as a function of filling are strongly indicative of a dependence

on the spin-valley polarization. We hope the characterization of the magnetic injection provided here, including its frequency, filling, and polarization dependence, as well as its approximate particle-hole constraints, will serve to unambiguously establish its existence in further experiments.

*Acknowledgements* - This work is supported by Grant PID2021-128760NB0-I00 from the Spanish MCIN/AEI/10.13039/501100011033/FEDER, EU.

- 
- [1] R. Bistritzer and A. H. MacDonald, *Proceedings of the National Academy of Sciences* **108**, 12233 (2011).
  - [2] Y. Cao, V. Fatemi, A. Demir, S. Fang, S. L. Tomarken, J. Y. Luo, J. D. Sanchez-Yamagishi, K. Watanabe, T. Taniguchi, E. Kaxiras, et al., *Nature* **556**, 80 (2018).
  - [3] X. Lu, P. Stepanov, W. Yang, M. Xie, M. A. Aamir, I. Das, C. Urgell, K. Watanabe, T. Taniguchi, G. Zhang, et al., *Nature* **574**, 653 (2019).
  - [4] A. Kerelsky, L. J. McGilly, D. M. Kennes, L. Xian, M. Yankowitz, S. Chen, K. Watanabe, T. Taniguchi, J. Hone, C. Dean, et al., *Nature* **572**, 95 (2019).
  - [5] Y. Xie, B. Lian, B. Jäck, X. Liu, C.-L. Chiu, K. Watanabe, T. Taniguchi, B. A. Bernevig, and A. Yazdani, *Nature* **572**, 101 (2019).
  - [6] P. Stepanov, M. Xie, T. Taniguchi, K. Watanabe, X. Lu, A. H. MacDonald, B. A. Bernevig, and D. K. Efetov, *Phys. Rev. Lett.* **127**, 197701 (2021).
  - [7] A. L. Sharpe, E. J. Fox, A. W. Barnard, J. Finney, K. Watanabe, T. Taniguchi, M. Kastner, and D. Goldhaber-Gordon, *Science* **365**, 605 (2019).
  - [8] M. Serlin, C. Tschirhart, H. Polshyn, Y. Zhang, J. Zhu, K. Watanabe, T. Taniguchi, L. Balents, and A. Young, *Science* **367**, 900 (2020).
  - [9] Y. Cao, D. Rodan-Legrain, J. M. Park, N. F. Yuan, K. Watanabe, T. Taniguchi, R. M. Fernandes, L. Fu, and P. Jarillo-Herrero, *science* **372**, 264 (2021).
  - [10] C.-C. Tseng, X. Ma, Z. Liu, K. Watanabe, T. Taniguchi, J.-H. Chu, and M. Yankowitz, *Nature Physics* **18**, 1038 (2022).
  - [11] Y. Cao, V. Fatemi, S. Fang, K. Watanabe, T. Taniguchi, E. Kaxiras, and P. Jarillo-Herrero, *Nature* **556**, 43 (2018).
  - [12] M. Yankowitz, S. Chen, H. Polshyn, Y. Zhang, K. Watanabe, T. Taniguchi, D. Graf, A. F. Young, and C. R. Dean, *Science* **363**, 1059 (2019).
  - [13] M. Oh, K. P. Nuckolls, D. Wong, R. L. Lee, X. Liu, K. Watanabe, T. Taniguchi, and A. Yazdani, *Nature* **600**, 240 (2021).
  - [14] Z. Zhang, J. Yang, B. Xie, Z. Feng, S. Zhang, K. Watanabe, T. Taniguchi, X. Yang, Q. Dai, T. Liu, et al., arXiv preprint arXiv:2408.12509 (2024).
  - [15] D. Wong, K. P. Nuckolls, M. Oh, B. Lian, Y. Xie, S. Jeon, K. Watanabe, T. Taniguchi, B. A. Bernevig, and A. Yazdani, *Nature* **582**, 198 (2020).
  - [16] K. P. Nuckolls, M. Oh, D. Wong, B. Lian, K. Watanabe, T. Taniguchi, B. A. Bernevig, and A. Yazdani, *Nature* **588**, 610 (2020).
  - [17] Y. Choi, H. Kim, Y. Peng, A. Thomson, C. Lewandowski, R. Polski, Y. Zhang, H. S. Arora, K. Watanabe,

- T. Taniguchi, et al., *Nature* **589**, 536 (2021).
- [18] Y. Choi, H. Kim, C. Lewandowski, Y. Peng, A. Thomson, R. Polski, Y. Zhang, K. Watanabe, T. Taniguchi, J. Alicea, et al., *Nature Physics* **17**, 1375 (2021).
- [19] U. Zondiner, A. Rozen, D. Rodan-Legrain, Y. Cao, R. Queiroz, T. Taniguchi, K. Watanabe, Y. Oreg, F. von Oppen, A. Stern, et al., *Nature* **582**, 203 (2020).
- [20] A. Rozen, J. M. Park, U. Zondiner, Y. Cao, D. Rodan-Legrain, T. Taniguchi, K. Watanabe, Y. Oreg, A. Stern, E. Berg, et al., *Nature* **592**, 214 (2021).
- [21] A. Datta, M. J. Calderon, A. Camjayi, and E. Bascones, *Nature Communications* **14**, 5036 (2023).
- [22] M. J. Calderón, A. Camjayi, A. Datta, and E. Bascones, “Cascades in transport and optical conductivity of twisted bilayer graphene,” (2024), [arXiv:2412.20855](https://arxiv.org/abs/2412.20855) [[cond-mat.str-el](https://arxiv.org/abs/2412.20855)].
- [23] M. Otteneder, S. Hubmann, X. Lu, D. A. Kozlov, L. E. Golub, K. Watanabe, T. Taniguchi, D. K. Efetov, and S. D. Ganichev, *Nano Letters* **20**, 7152 (2020).
- [24] S. Hubmann, P. Soul, G. Di Battista, M. Hild, K. Watanabe, T. Taniguchi, D. K. Efetov, and S. D. Ganichev, *Phys. Rev. Mater.* **6**, 024003 (2022).
- [25] C. Ma, S. Yuan, P. Cheung, K. Watanabe, T. Taniguchi, F. Zhang, and F. Xia, *Nature* **604**, 266 (2022).
- [26] N. C. Hesp, I. Torre, D. Barcons-Ruiz, H. Herzig Sheinfux, K. Watanabe, T. Taniguchi, R. Krishna Kumar, and F. H. Koppens, *Nat. Commun.* **12**, 1640 (2021).
- [27] S. S. Sunku, D. Halbertal, T. Stauber, S. Chen, A. S. McLeod, A. Rikhter, M. E. Berkowitz, C. F. B. Lo, D. E. Gonzalez-Acevedo, J. C. Hone, et al., *Nat. Commun.* **12**, 1641 (2021).
- [28] J. Liu and X. Dai, *npj Comp. Mater.* **6**, 57 (2020).
- [29] D. Kaplan, T. Holder, and B. Yan, *Phys. Rev. Res.* **4**, 013209 (2022).
- [30] S. Zhang, X. Lu, and J. Liu, *Phys. Rev. Lett.* **128**, 247402 (2022).
- [31] S. Chaudhary, C. Lewandowski, and G. Refael, *Phys. Rev. Res.* **4**, 013164 (2022).
- [32] A. Arora, J. F. Kong, and J. C. W. Song, *Phys. Rev. B* **104**, L241404 (2021).
- [33] F. Peñaranda, H. Ochoa, and F. de Juan, *Phys. Rev. Lett.* **133**, 256603 (2024).
- [34] A. Postlewaite, A. Raj, S. Chaudhary, and G. A. Fiete, “Nonlinear optical responses and quantum geometry in rhombohedral trilayer graphene,” (2024), [arXiv:2407.03404](https://arxiv.org/abs/2407.03404) [[cond-mat.mes-hall](https://arxiv.org/abs/2407.03404)].
- [35] R. K. Kumar, G. Li, R. Bertini, S. Chaudhary, K. Nowakowski, J. M. Park, S. Castilla, Z. Zhan, P. A. Pantaleón, H. Agarwal, S. Battle-Porro, E. Icking, M. Ceccanti, A. Reserbat-Plantey, G. Piccinini, J. Barrier, E. Khestanova, T. Taniguchi, K. Watanabe, C. Stampfer, G. Refael, F. Guinea, P. Jarillo-Herrero, J. C. W. Song, P. Stepanov, C. Lewandowski, and F. H. L. Koppens, “Terahertz photocurrent probe of quantum geometry and interactions in magic-angle twisted bilayer graphene,” (2024), [arXiv:2406.16532](https://arxiv.org/abs/2406.16532) [[cond-mat.mes-hall](https://arxiv.org/abs/2406.16532)].
- [36] Y. Zhang, T. Holder, H. Ishizuka, F. de Juan, N. Nagaosa, C. Felser, and B. Yan, *Nature communications* **10**, 3783 (2019).
- [37] R. Fei, W. Song, and L. Yang, *Phys. Rev. B* **102**, 035440 (2020).
- [38] H. Wang and X. Qian, *npj Comput. Mater.* **6**, 199 (2020).
- [39] J. Ahn, G.-Y. Guo, and N. Nagaosa, *Phys. Rev. X* **10**, 041041 (2020).
- [40] T. Holder, D. Kaplan, and B. Yan, *Phys. Rev. Research* **2**, 033100 (2020).
- [41] H. Watanabe and Y. Yanase, *Phys. Rev. X* **11**, 011001 (2021).
- [42] H. Watanabe and Y. Yanase, *Phys. Rev. B* **104**, 024416 (2021).
- [43] M. Merte, F. Freimuth, T. Adamantopoulos, D. Go, T. G. Saunderson, M. Kläui, L. Plucinski, O. Gomonay, S. Blügel, and Y. Mokrousov, [arxiv:2109.10192](https://arxiv.org/abs/2109.10192) (2021).
- [44] S. Okumura, T. Morimoto, Y. Kato, and Y. Motome, [arXiv:2108.00674](https://arxiv.org/abs/2108.00674) (2021).
- [45] C. Aversa and J. E. Sipe, *Phys. Rev. B* **52**, 14636 (1995).
- [46] L. E. Golub, S. A. Tarasenko, M. V. Entin, and L. I. Magarill, *Phys. Rev. B* **84**, 195408 (2011).
- [47] N. Bultinck, E. Khalaf, S. Liu, S. Chatterjee, A. Vishwanath, and M. P. Zaletel, *Phys. Rev. X* **10**, 031034 (2020).
- [48] Y. H. Kwan, G. Wagner, T. Soejima, M. P. Zaletel, S. H. Simon, S. A. Parameswaran, and N. Bultinck, *Phys. Rev. X* **11**, 041063 (2021).
- [49] Y. Zhang, K. Jiang, Z. Wang, and F. Zhang, *Phys. Rev. B* **102**, 035136 (2020).
- [50] J. Liu and X. Dai, *Phys. Rev. B* **103**, 035427 (2021).
- [51] M. Xie and A. H. MacDonald, *Phys. Rev. Lett.* **124**, 097601 (2020).
- [52] N. Bultinck, S. Chatterjee, and M. P. Zaletel, *Phys. Rev. Lett.* **124**, 166601 (2020).
- [53] J. Kang and O. Vafek, *Phys. Rev. Lett.* **122**, 246401 (2019).
- [54] F. Xie, A. Cowsik, Z.-D. Song, B. Lian, B. A. Bernevig, and N. Regnault, *Phys. Rev. B* **103**, 205416 (2021).
- [55] J. Kang and O. Vafek, *Phys. Rev. B* **102**, 035161 (2020).
- [56] S. Liu, E. Khalaf, J. Y. Lee, and A. Vishwanath, *Phys. Rev. Res.* **3**, 013033 (2021).
- [57] F. Xie, J. Kang, B. A. Bernevig, O. Vafek, and N. Regnault, *Phys. Rev. B* **107**, 075156 (2023).
- [58] Y.-Z. Chou and S. Das Sarma, *Phys. Rev. Lett.* **131**, 026501 (2023).
- [59] H. Hu, G. Rai, L. Crippa, J. Herzog-Arbeitman, D. Călugăru, T. Wehling, G. Sangiovanni, R. Valentí, A. M. Tsvelik, and B. A. Bernevig, *Phys. Rev. Lett.* **131**, 166501 (2023).
- [60] G.-D. Zhou, Y.-J. Wang, N. Tong, and Z.-D. Song, *Phys. Rev. B* **109**, 045419 (2024).
- [61] G. Rai, L. Crippa, D. Călugăru, H. Hu, F. Paoletti, L. de’ Medici, A. Georges, B. A. Bernevig, R. Valentí, G. Sangiovanni, and T. Wehling, *Phys. Rev. X* **14**, 031045 (2024).
- [62] P. Moon and M. Koshino, *Phys. Rev. B* **87**, 205404 (2013).
- [63] E. S. Morell, L. Chico, and L. Brey, *2D Materials* **4**, 035015 (2017).
- [64] J. Ahn and N. Nagaosa, *Nature communications* **12**, 1617 (2021).
- [65] Z. Song, Z. Wang, W. Shi, G. Li, C. Fang, and B. A. Bernevig, *Phys. Rev. Lett.* **123**, 036401 (2019).
- [66] Z.-D. Song, B. Lian, N. Regnault, and B. A. Bernevig, *Phys. Rev. B* **103**, 205412 (2021).
- [67] B. A. Bernevig, Z.-D. Song, N. Regnault, and B. Lian, *Phys. Rev. B* **103**, 205413 (2021).
- [68] Z.-D. Song and B. A. Bernevig, *Phys. Rev. Lett.* **129**, 047601 (2022).
- [69] J. M. B. Lopes dos Santos, N. M. R. Peres, and A. H.

- Castro Neto, *Phys. Rev. B* **86**, 155449 (2012).
- [70] To ensure periodicity in the Moiré Brillouin zone in bandstructure calculations, one can safely assume the  $\Lambda_C \rightarrow \infty$  without affecting the low energy physics and, then, truncate the plane-wave basis expansion in Moiré reciprocal lattice vectors to the first shell.
- [71] P. Moon and M. Koshino, *Phys. Rev. B* **90**, 155406 (2014).
- [72] M. Long, Z. Zhan, P. A. Pantaleón, J. A. Silva-Guillén, F. Guinea, and S. Yuan, *Phys. Rev. B* **107**, 115140 (2023).
- [73] Y. H. Kwan, S. A. Parameswaran, and S. L. Sondhi, *Phys. Rev. B* **101**, 205116 (2020).
- [74] A. L. Sharpe, E. J. Fox, A. W. Barnard, J. Finney, K. Watanabe, T. Taniguchi, M. A. Kastner, and D. Goldhaber-Gordon, *Nano letters* **21**, 4299 (2021).
- [75] O. Antebi, A. Stern, and E. Berg, *Phys. Rev. B* **105**, 104423 (2022).
- [76] Y. Su and S.-Z. Lin, *Phys. Rev. Lett.* **125**, 226401 (2020).
- [77] W.-Y. He, D. Goldhaber-Gordon, and K. T. Law, *Nature communications* **11**, 1650 (2020).
- [78] X. Ying, M. Ye, and L. Balents, *Phys. Rev. B* **103**, 115436 (2021).
- [79] S. Chatterjee, N. Bultinck, and M. P. Zaletel, *Phys. Rev. B* **101**, 165141 (2020).
- [80] J. Shi, J. Zhu, and A. H. MacDonald, *Phys. Rev. B* **103**, 075122 (2021).
- [81] S. Grover, M. Bocarsly, A. Uri, P. Stepanov, G. Di Battista, I. Roy, J. Xiao, A. Y. Meltzer, Y. Myasoedov, K. Pareek, et al., *Nature physics* **18**, 885 (2022).